

1 This manuscript was submitted to The Seismic Record 9/15/2023. Results should be considered preliminary until
2 thoroughly peer reviewed.

3 **FAULT SLIP POTENTIAL NEAR THE DEADLY M_w 6.8 OUKAÏMEDENE, MOROCCO EARTHQUAKE**

4 Will Levandowski, Tetra Tech, Inc.

5 Will.Levandowski@tetrtech.com

6

7 **Abstract**

8 Thousands were killed by the September 8, 2023, M_w 6.8 Oukaïmedene, Morocco earthquake in the Western High
9 Atlas. To determine the fault orientations most likely to host aftershocks and future large earthquakes, the
10 regional crustal stress field is estimated by inverting focal mechanisms from the High/Middle Atlas junction area,
11 Central, and Western High Atlas, and the associated fault slip potential is modeled. North-south shortening is
12 accommodated by roughly equal parts reverse and strike-slip motion. As such, many fault orientations are
13 optimally aligned for slip: steep NE-, SW-, SSE-, or NNW-striking planes, gently (\sim 15–40°) dipping east- and
14 west-striking planes, and orientations between. Aftershocks are most likely to be triggered on these faults, while
15 steep E–W and nearly all N–S faults are relatively more stable.

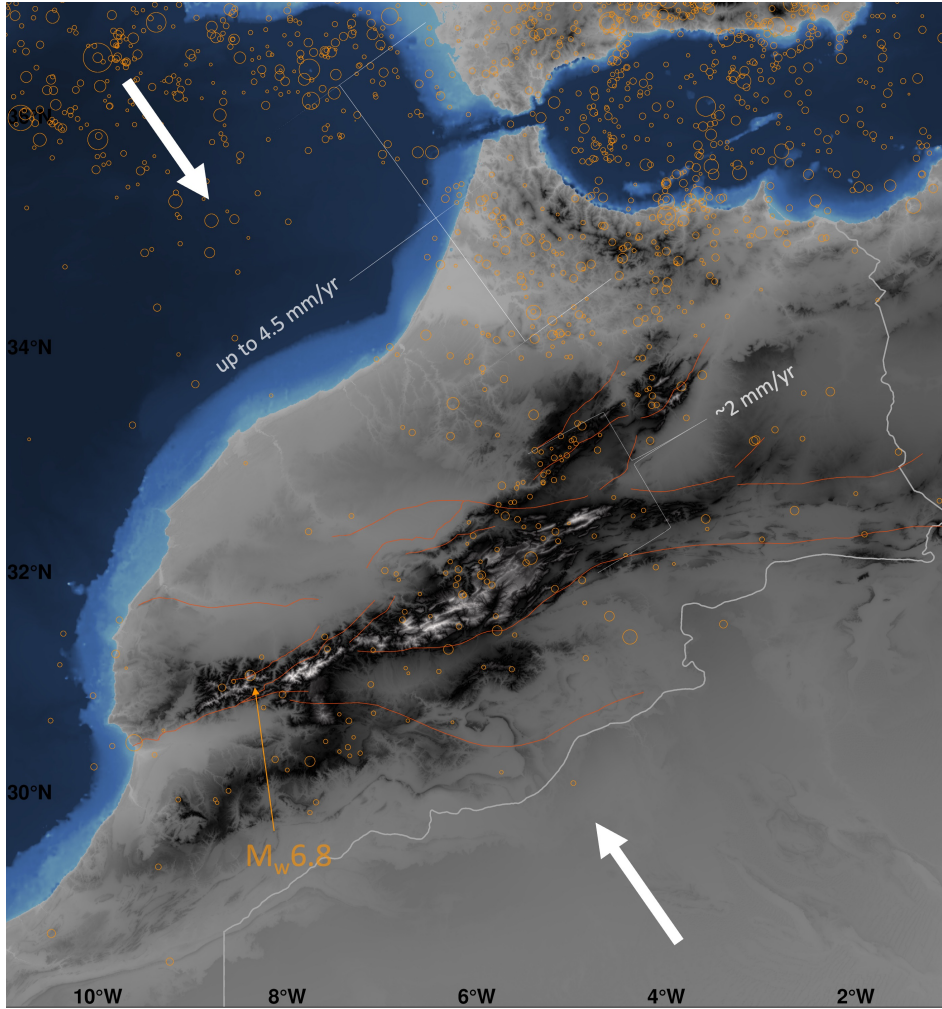
16

17 **Introduction**

18 Rapidly characterizing the stress field and locally favorable fault orientations may identify faults that are
19 most likely to host aftershocks during an ongoing seismic sequence. An investigation of the crustal stress field
20 near the epicenter of the 8 September 2023 M_w 6.8 Oukaïmedene, Morocco earthquake (**Figure 1**) and associated
21 fault slip potential (FSP) models are presented here. Crustal stress is determined by inversions of earthquake focal
22 mechanisms from the western to central High Atlas and the High/Middle Atlas junction (**Figure 2**). The resulting
23 stress tensors are input to FSP models, which quantify the suitability for slip in the local stress field as a function
24 of fault orientation. These quantifications should identify the fault orientations most likely to host aftershocks in
25 the coming days to weeks, as well as future mainshocks.

26 With nearly 3,000 people already known to have died, the M_w 6.8 earthquake is the deadliest in Morocco
27 since the 1960 M5.9 in Agadir (**Figure 2**). Moment tensors from the USGS NEIC and Quick CMT indicate

28 moderately steep WSW- and gently dipping ESE-striking nodal planes ($N255E$, 69° – 73° and $N122E$, 29° : see
29 Data and Resources). These planes were used by USGS in finite-fault models jointly constrained by InSAR and
30 teleseismic waveforms (see Data and Resources). Hypocentral depths range from 26 to 33 km across these
31 models.



32
33 **Figure 1: Overview** of regional tectonics. Red-orange lines: Major faults within the main study region digitized from El
34 Moudnib et al. (2023). Orange circles: Seismicity 1522–2005 (Peláez et al., 2007). White arrows indicate the approximate
35 Africa-Eurasia convergence direction.
36
37

38 **Setting**

39 Morocco marks the SW corner of the vast Alpine-Himalayan orogen, and strain in the High Atlas marks
40 the southernmost extent of this shortening. As the African plate converges obliquely NNW with the Eurasian
41 plate, some 4.5 mm/yr of shortening are absorbed by the Rif Mountains in northernmost Morocco and Algeria.
42 Meanwhile 2 mm/yr are transmitted ~500 km south of the plate boundary to the Atlas Mountains system (Azzouzi
43 et al. 2005).

44 From north to south, the Atlasic domains comprise the NE-trending Middle Atlas, E-trending eastern High
45 Atlas, ENE-trending central High Atlas, and NE-trending western High Atlas, all of which are bounded by locally
46 range-parallel thrust faults (**Figure 1**). From the central High Atlas (e.g., High/Middle Atlas junction) to the western
47 High Atlas, including near the epicenter, these thrusts rotate from nearly perpendicular to shortening to oblique to
48 shortening. As a result, deformation appears to transition from dominantly reverse faulting with a minor strike-slip
49 component in the more seismically active High-Middle Atlas junction (El Moudnib et al., 2023) to oblique faulting
50 near the epicenter and westward through Agadir (**Figure 2**).

51

52

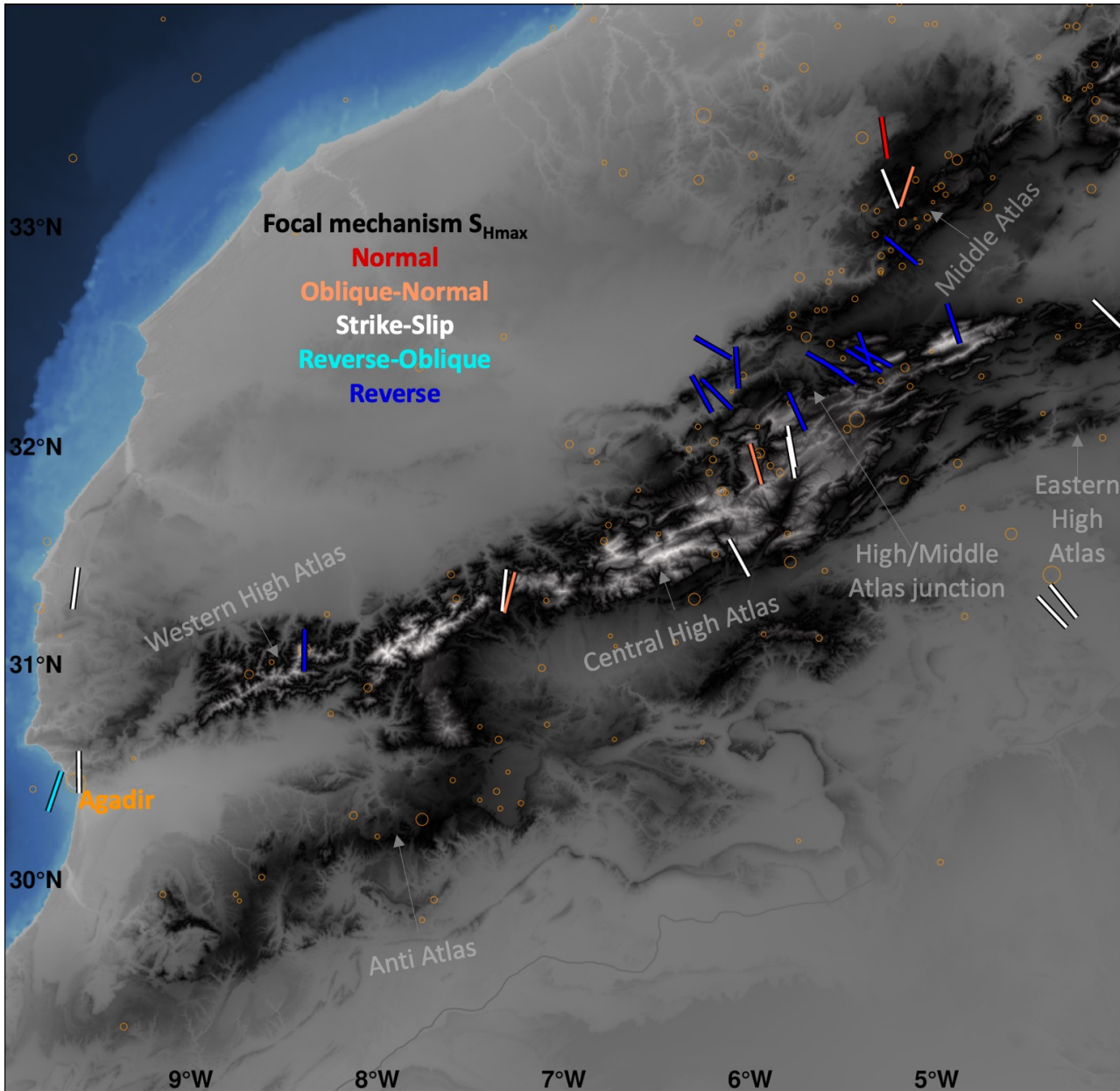
53

54

55

56

57



58 **Figure 2: Focal mechanisms** within the study area depicted as bars oriented in the maximum horizontal shortening direction
 59 and color-coded by faulting style (following the convention of Zoback, 1992).

60
 61 **Crustal Stress**

62 *Previous Work and Data*

63 Focal mechanisms have been compiled by Medina (2008) for all of Morocco and more recently by El
 64 Moudnib et al. (2023) for the High/Middle Atlas Junction area. Hatzfeld et al. (1977) provided a solution for the

65 1960 Agadir earthquake. Several events have moment tensors available from the global CMT project, GFZ-
66 Geofon, USGS, and INGV. No additional data are available from the World Stress Map (Heidbach et al., 2016).

67 With sparse historical to instrumental seismicity in the epicentral, a rather expansive region (**Figure 2**)
68 from -10° to -4° longitude and 28° to 34° latitude is examined (data from farther west and south would be
69 included, but none were found), availing focal mechanisms for 28 earthquakes. With caution that a single focal
70 mechanism—or even a few—does not constrain the local stress tensor (e.g., McKenzie, 1969), these display some
71 coherent geographic patterns. All have NW- to N-trending maximum shortening directions $S_{H\max}$ (the P-axis for
72 reverse to strike-slip events), consistent with regional strain. In the Central and Western High Atlas, strike-slip
73 faulting is dominant, and P-axes trend approximately north. Reverse faulting mechanisms with NW-trending P-
74 axes typify the High/Middle Atlas junction area. Three mechanisms in the Middle Atlas display a variety of
75 faulting styles and $S_{H\max}$, while three mechanisms from the Eastern High Atlas and south have strike-slip
76 mechanisms with NW-trending P-axes. These latter two may reflect different states of stress from that near
77 Oukaimedene and are thus preferably omitted from the analysis.

78 El Moudnib et al. (2023) derived 15 focal mechanisms near the High/Middle Atlas junction, which they
79 combined with several others from the southern Middle Atlas, Eastern and Central High Atlas, and areas to the
80 southeast in a single stress inversion. The best-fit tensor favors nearly pure reverse faulting with N–S shortening
81 (the $A\phi$ parameter described below equals 2.5 ± 0.1 , with $S_{H\max}$ N2E). The present analysis focuses on the Western
82 High Atlas, some 300 km southwest of El Moudnib et al.’s focus, and includes four additional mechanisms from
83 that area.

84

85 *Stress Inversions*

86 Inversions of focal mechanisms are well established and stem from the axiom that coseismic slip parallels
87 the shear traction resolved on the fault plane (e.g., Angelier, 1979). The latter depends linearly on fault orientation
88 and the 3D stress tensor. Under the condition that the selected earthquakes all occurred under the same stress
89 field, this linear system quickly becomes overdetermined with multiple slip observations from faults of different
90 orientations. Inverting this linear system solves for the 3D stress tensor that minimizes the angular misfit between

91 the slip vectors and shear traction on the respective fault planes. By convention, 20 or more focal mechanisms are
92 needed for reliable stress inversions (e.g., Townend and Zoback, 2004).

93 The normalized stress tensor can be fully described in terms of the directions and ratio of magnitudes of
94 the principal stresses ϕ :

95
$$\phi = (S_2 - S_3) / (S_1 - S_3) \quad (1)$$

96
97 with S_1 the magnitude of the maximally compressive stress, S_2 intermediate, and S_3 the minimum.

98 Simpson (1997) combined ϕ with the style of faulting (normal/strike-slip/reverse, as defined by principal
99 axis plunges; Zoback, 1992) to describe the style of deformation as a quantity $A\Phi$:

100
101
$$A\Phi = (n + 0.5) + (-1)^n(\phi - 0.5) \quad (2)$$

102
103 In equation 2, $n=0$ for normal faulting, 1 for strike-slip, and 2 for thrust. Consequently, $A\Phi$ defines a continuum
104 from radial extension ($A\Phi = 0$) to radial contraction ($A\Phi = 3$), passing through: uniaxial extension/pure normal
105 faulting ($A\Phi=0.5$); oblique extension ($A\Phi=1.0$); horizontal shear/strike-slip ($A\Phi=1.5$); oblique contraction
106 ($A\Phi=2.0$), and uniaxial contraction/pure reverse faulting, ($A\Phi=2.5$).

107 The inversion algorithm (following Levandowski et al., 2018a) assesses uncertainty with 1001 Monte
108 Carlo realizations. Each realization jackknife-resamples the dataset (discarding $n_{\text{mechanisms}}^{0.5}$), randomly perturbs
109 the individual slip vectors by $\pm 15^\circ$ and chooses a random coefficient of friction between 0.3 and 0.9. The retained
110 mechanisms are then iteratively inverted (following Vavryčuk, 2014), selecting the less stable of the two nodal
111 planes for each event with respect to the current estimate of the stress tensor, inverting these mechanisms for an
112 updated stress estimate, and recomputing the stability of each plane, for a total of 5 iterations per realization. A
113 total of 1001 realizations are used for the inversion, and the values discussed are the median \pm one standard
114 deviation.

115 The preferred set of mechanisms is geographically limited to the High/Middle Atlas junction, Central and
116 Western High Atlas (south of 32.75° latitude and west of -4.5° longitude) and comprises 21 mechanisms (**Figure**

117 **S1).** In the preferred approach, the individual mechanisms are weighted by inverse-distance from the M6.8
118 epicenter. Inversions under nine different parameterizations are summarized in **Table S1** (Models 0–8): Results
119 are relatively insensitive to the inversion setup. Details of the focal mechanisms are provided in **Table S2**.

120 Inverting the preferred set yields a reverse-oblique faulting regime ($A\phi=2.07\pm0.15$) that accommodates
121 north-south horizontal shortening N2E ($\pm5^\circ$) (**Figure 3**). Fit to the mechanisms is acceptable, with average
122 angular misfit 25.5° between the shear traction on each respective focal plane and the slip vector on the iteratively
123 selected focal plane. A value of $40\text{--}45^\circ$ is often taken as a threshold for homogenous stress (Michael et al., 1990;
124 Michael, 1991). By contrast, the auxiliary planes mismatch by an average of 43° .

125

Oukaimedene: Oblique shortening

$A\phi=2.07\pm0.15$

σ_{max} N2E $\pm5^\circ$

n=21

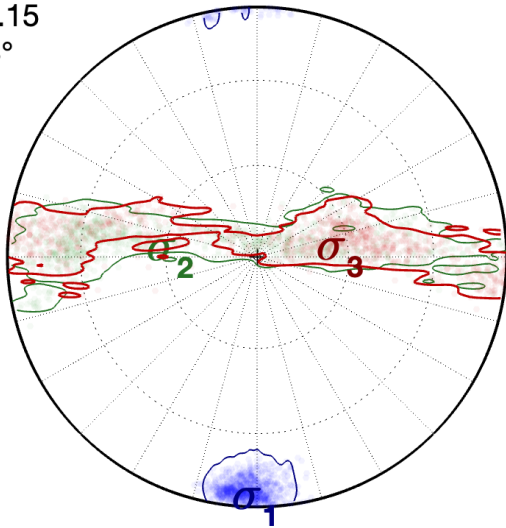


Figure 3: Stress inversion results Lower hemisphere projection of principal stress axes from 1001 inversions. The maximum compressive stress in the western High Atlas and environs is horizontal and north/south. The other two stresses (horizontal, east/west and sub-vertical) are approximately equal in magnitude. This stress promotes north-south shortening by a nearly even mix of reverse and strike-slip

137 faulting.

138

139

140

141 Fault Slip Potential Modeling

142 FSP modeling provides a quantitative metric for how well faults are oriented for frictional slip in the local
143 stress field. From the normalized stress tensors derived from focal mechanism inversions, the full stress tensors

144 are calculated (following Walsh and Zoback, 2016; Levandowski et al., 2018b) at a nominal depth, here 5 km.

145 The shear and normal tractions are computed as functions of fault orientation (strike and dip), and the suitability
146 of faults for slip is then quantified in terms of distance from Coulomb failure, or the difference between the
147 computed shear traction magnitude and the frictional resistance:

148

$$dCFS = \text{friction} \times |\text{effective normal traction}| - |\text{shear traction}| \quad (3)$$

150

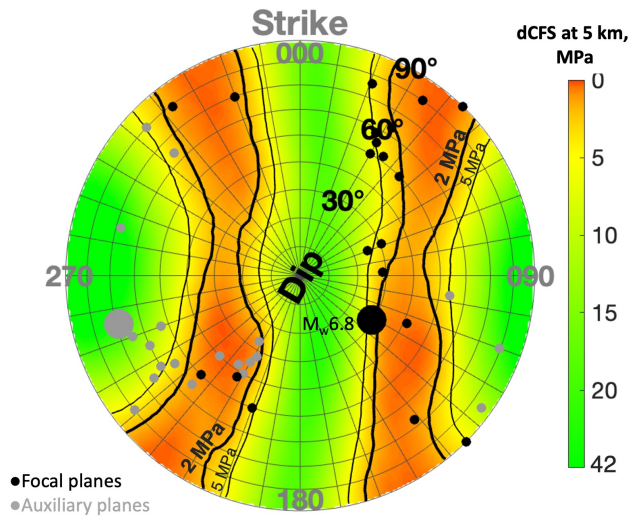
151 Thus, dCFS represents the shear stress increase that may trigger slip on a pre-existing fault. The
152 underlying assumption of FSP modeling is that the crust is in a state of frictional failure equilibrium (e.g., Zoback,
153 2010), meaning that at least one fault in the local stress field has $dCFS = 0$ MPa.

154 Because FSP under a given stress depends only on the fault strike and dip, it provides a complementary
155 constraint to stress inversions, which treat strike and dip as fixed and minimize misfit to slip vectors (rake). This
156 combination can be also used to disambiguate the focal and auxiliary planes and choose from different focal
157 mechanism solutions for a single event (Levandowski et al., 2023).

158 The Monte Carlo-style stress inversions provide 1001 estimates of the normalized stress tensor. Each of
159 these 1001 models and its attendant friction are used to compute the full stress tensor and then the shear and
160 normal tractions and dCFS for all possible fault planes (following the approach of Levandowski et al., 2018b;
161 2023). Overburden density is varied randomly across the 1001 realizations from 2650 to 2850 kg/m³. Pore
162 pressure is set to hydrostatic. The values of dCFS discussed here are the 95% confidence lower bound: in 5% of
163 Monte Carlo trials, this increase in CFS (or less) would trigger instability on the fault plane in question.

164

This 95% confidence lower bound averages 2.8 MPa on the iteratively selected focal planes (**Figure 4**,



165 black dots). For comparison, in cases of induced seismicity, most events are retrospectively found to have occurred on faults within ~2 MPa of failure (also for a nominal depth of 5 km; Walsh & Zoback, 2016). The auxiliary planes are comparatively far from failure, with average 95% confidence dCFS of 7.1 MPa (**Figure 4**, gray dots).

175

Figure 4: Fault slip potential quantified in terms of dCFS (Coulomb stress change to instability, Equation 3). The values shown are the 95% lower confidence bound across 1001 inversions for faults oriented as described by the strike and dip polar axes. The iteratively selected focal planes for the best-fit stress are shown as black dots. Their auxiliary planes are shown as gray dots. Large dots denote the Oukaïmedene earthquake. The ESE-striking, gently dipping nodal plane is well aligned in the regional stress field (dCFS=3.6 MPa), while the N255E plane appears poorly oriented (dCFS=22.6 MPa).

180

181

182

183

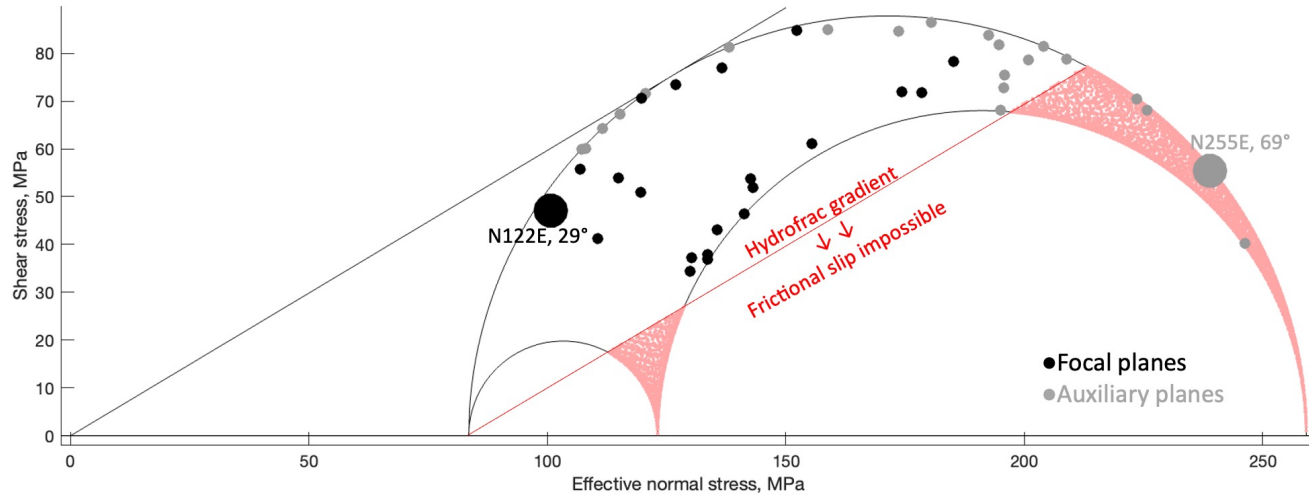
Results

184

In regions with mixed modes of faulting, many fault orientations are potentially active (Levandowski et al., 2018b). The ~N–S oblique shortening in the western High Atlas can be accomplished by strike-slip on steep faults striking NE, SW, SSE, or NNW, by reverse motion on gently (~30°) dipping faults striking east/west, or by oblique slip on orientations between these (**Figure 4**). High FSP (low dCFS) faults thus form two continua rather than two (reverse and normal) or four (strike-slip) isolated optimal orientations.

189 This diversity notwithstanding, many orientations are not favorable for slip, including NNW–SSE faults
190 of any dip and E–W faults any steeper than $\sim 50^\circ$. Indeed, the iterative focal/auxiliary plane determination
191 (Vavryčuk, 2014) does not select a steep E–W fault for any of the events.

192 Seismic moment tensors of the $M_w 6.8$ feature a gently dipping ESE-striking plane well oriented for
193 reverse-oblique faulting under north-south shortening and a WSW-striking fault that is quite steep (dip 69°)
194 relative to the maximum stress vector derived here. Indeed, the N255E plane (large gray dot in **Figure 4**) is at
195 least 21.9 MPa from failure in 95% of the models while its N122E complement (large black dot in **Figure 4**) may
196 be within 3.6 MPa (**Figure 5**). Given only these two choices, stress considerations favor the ESE-striking plane as
197 the causative fault.



198
199
200 **Figure 5: Mohr Circle** for the single best-fit stress tensor under the preferred inversion scheme. Red indicates the area
201 beyond the hydrofracture gradient, which is incompatible with frictional slip. The ESE-striking nodal plane (large black dot) is
202 well aligned for slip, while the WSW-striking plane lies beyond the hydrofracture gradient for this specific stress tensor. Note
203 that 1001 tensors were developed under this inversion setup, and this plane is not slip-incompatible in all models under this or
204 other parameterizations (see Table S1).

205
206 This finding contrasts with the finite fault model developed jointly from InSAR and seismic waveforms
207 (see Data and Resources) in which the WSW-striking plane provides superior fit, especially to surface waves

208 (Yeck, written communication 2023– see Acknowledgements). To determine whether other parameterizations or
209 focal mechanism groupings would favor this plane, a variety of additional cases were considered (**Table S1**).
210 These include imposing low-friction faults (**Figure S2**), allowing only the SW-striking nodal planes to be selected
211 (**Figure S3**), and both. Still, the ESE nodal plane remains closer to failure ($dCFS = 2.2 \text{ MPa}$) than the WSW plane
212 (5.5 MPa) (**Figure S4**). It is important to note that the finite-fault model is sensitive to the slip realized during the
213 earthquake, while the stress estimates most specifically pertain to rupture nucleation.

214 The major, active range-bounding faults mostly strike SW to WSW. Indeed, **Figure 4** indicates that
215 WSW-striking faults with $\sim 15\text{--}40^\circ$ dips may be optimally oriented, while SW-striking faults with dips anywhere
216 from $\sim 20^\circ$ to 90° could be optimally aligned. The regional fault system comprises numerous sub-parallel strands
217 (**Figure 1**), presumably with varying dips and variable dip with depth. Rupture nucleation would be most likely
218 on a patch with favorable orientation—either a gentler WSW- or similarly steep SW-striking fault—but could
219 have propagated up-dip onto steeper sections or laterally onto more westerly segments (Goldberg, written
220 communication 2023– see Acknowledgements). Thus, the discrepancy does not impugn the finite-fault model or
221 moment tensors but rather presents the possibility that slip occurred on a curved surface or multiple neighboring
222 patches.

223 A second possibility is that stress differs in the Western High Atlas from areas farther east, where most of
224 the available data comes from. This local stress may not be adequately modeled because of the paucity of data
225 near Oukaimedene. Inversions were conducted (Models 9–11, **Table S1**, **Figure S1**) for progressively smaller
226 areas around the epicenter, although with fewer mechanisms— $n=15, 10$, and 6 —than needed for a reliable result.
227 Doing so (**Figure S5**) progressively decreases $A\phi$ and increases the slip potential of the WSW nodal plane. At the
228 extreme, with only the 6 mechanisms from the Western High Atlas (Model 11), the median stress regime
229 approaches pure strike-slip, $A\phi=1.59\pm0.24$, and the two nodal planes are approximately equally likely to slip.
230 Thus, with insufficient data, it remains permissible that the stress regime in the Western High Atlas transitions to
231 favor strike-slip more heavily and thus allows reactivation of a moderately steep WSW-striking nodal plane.

232

233

234

235 **Conclusions**

236 The crustal stress field across the Central and Western High Atlas is characterized by north-south
237 maximal compression and favors a mix of reverse, reverse-oblique, and strike-slip faulting. Several fault
238 orientations are well oriented for slip in the modern stress field (**Figure 4**) and are thus likely to host aftershocks
239 or future ruptures: east-west reverse faults dipping ~15–40°, steep NE–SW or SSE–NNW strike-slip faults, and
240 reverse-oblique faults between these orientations. By contrast, east-west planes dipping more than ~50° and
241 nearly all north-south faults appear unlikely to slip.

242 Moment tensor nodal planes from the M_w 6.8 Oukaïmedene earthquake are oriented N122E, 29° and
243 N255E, 69°. Fault slip potential calculations find the latter to be too steep (or too westerly) to be well-aligned for
244 slip, yet a finite fault model finds significantly better fit to waveforms and InSAR with this plane than the former.
245 Further, the regional range-bounding fault network comprises multiple sub-parallel SW- to WSW-striking strands.
246 The slip potential models indicate that WSW-striking faults dipping ~15–40° and SW-striking faults of nearly
247 any dip may be optimally oriented. Thus, it is plausible that rupture nucleated on a less steep or more
248 southwesterly patch within thrust fault network and propagated onto the segment identified by moment tensors
249 and the finite fault model. A second possibility is that stress in the Western High Atlas differs from areas farther
250 east, where most of the available focal mechanisms are. Western High Atlas data are limited to six mechanisms,
251 and inverting these permits that strike-slip faulting becomes dominant such that the ESE plane and steeper WSW
252 plane are equally likely to rupture. Inversions with so few data are not reliable, however, so ongoing studies of
253 surface deformation, aftershock distribution, and focal mechanisms will be needed to resolve local stress in the
254 Western High Atlas.

255

256 **Acknowledgments**

257 The author thanks Dara Goldberg and Will Yeck (USGS) for helpful discussion of the finite-fault model.

258

259 **Data and Resources**

260 Focal mechanism details are provided in Table S2 and are available in the referenced literature. Oukaïmedene
261 moment tensors from (<https://earthquake.usgs.gov/earthquakes/eventpage/us7000kufc/moment-tensor>, last
262 accessed 12 September 2023) and Global CMT (<https://www.globalcmt.org/CMTsearch.html>, last accessed 11
263 September 2023) (Dziewonski et al., 1981; Ekstrom et al., 2012). Finite fault model from
264 (<https://earthquake.usgs.gov/earthquakes/eventpage/us7000kufc/finite-fault>, last accessed September 14, 2023).

265 Stress inversion and FSP codes are available at github.com/WillLevandowski/

266

267 **Declaration of competing interests**

268 The author declares no competing interests.

269

270 **References**

271 Angelier, J. (1979) Determination of the mean principal stresses for a given fault population, Tectonophysics 56,
272 T17-T26, 1979.

273 Angelier, J. (1990) Inversion of field data in fault tectonics to obtain the regional stress, III, A new rapid direct
274 inversion method by analytical means, GeophysJ. . Int., 103, 363-376, 1990.

275 Azzouzi, R., M. Ettarid, H. Semlali, A. Rimi, A. Trache, M. Aït Belaid, and L. Aït Brahim (2005). Actual
276 horizontal displacements and parametric deformation determinations of African and Eurasian tectonic
277 plates in the Western Mediterranean region. Workshop on Fracture Dynamics: Theory and Applications
278 to Earthquakes.

279 Dziewonski, A. M., T.-A. Chou and J. H. Woodhouse (1981) Determination of earthquake source parameters
280 from waveform data for studies of global and regional seismicity, J. Geophys. Res., 86, 2825-2852.

281 doi:10.1029/JB086iB04p02825

- 282 El Moudnib, L., Timoulali, Y., Nouayti, A., El Abbassi, M., Bouka, M., Nouayti, N., & Mhammdi, N. (2023).
283 Seismotectonic model of High-Middle Atlas Junction (Morocco) derived from earthquake focal
284 mechanism and stress tensor analysis. *Modeling Earth Systems and Environment*, 9(2), 2407-2423.
- 285 Ekström, G., M. Nettles, and A. M. Dziewonski (2012) The global CMT project 2004-2010: Centroid-moment
286 tensors for 13,017 earthquakes, *Phys. Earth Planet. Inter.*, 200-201, 1-9, doi:10.1016/j.pepi.2012.04.002
- 287 Hatzfeld D., Frogneux M. & Girardin N. 1977. Etude de la sismicité dans la région de l'arc de Gibraltar et
288 l'Algérie du Nord. *Bull. Soc. Géol. Fr.*, (7), XIX, n°4, 741-747.
- 289 Heidbach, O., M. Rajabi, X. Cui, K. Fuchs, B. Müller, J. Reinecker, K. Reiter, M. Tingay, F. Wenzel, F. Xie, M.
290 O. Ziegler, M.-L. Zoback, and M. D. Zoback (2018): The World Stress Map database release 2016:
291 Crustal stress pattern across scales. *Tectonophysics*, 744, 484-498, doi:10.1016/j.tecto.2018.07.007
- 292 Heidbach, Oliver; Rajabi, Mojtaba; Reiter, Karsten; Ziegler, Moritz, WSM Team (2016): World Stress
293 Map Database Release 2016. GFZ Data Services, doi:10.5880/WSM.2016.00
- 294 Levandowski, W., Weingarten, M., and Walsh F.R. III. (2018) Geomechanical sensitivities of injection-induced
295 earthquakes: *Geophysical Research Letters*, v. 45, [doi:10.1029/2018GL077551](https://doi.org/10.1029/2018GL077551)
- 296 Levandowski, W., Herrmann, R.B., Briggs, R., Boyd, O.S., and Gold, R. (2018) A revised stress map of the
297 continental United States reveals evidence for heterogeneous intraplate stress: *Nature Geoscience*, v. 11,
298 doi:10.1038/s41561-018-0120-x.
- 299 Levandowski, W., C. Powell, M. Chapman, and Q. Wu (2023). Anomalous Crustal Stress in the Eastern
300 Tennessee Seismic Zone, *Seismol. Res. Lett.* XX, 1–13, doi: 10.1785/0220220364.
- 301 Michael, A. J., Ellsworth, W. L., & Oppenheimer, D. H. (1990). Coseismic stress changes induced by the 1989
302 Loma Prieta, California earthquake. *Geophysical Research Letters*, 17(9), 1441-1444
- 303 Michael, A. J. (1991). Spatial variations in stress within the 1987 Whittier Narrows, California, aftershock
304 sequence: New techniques and results. *Journal of Geophysical Research: Solid Earth*, 96(B4), 6303-
305 6319.

- 306 McKenzie, D. P. (1969). The relation between fault plane solutions for earthquakes and the directions of the
307 principal stresses. *Bulletin of the Seismological Society of America*, 59(2), 591-601.
- 308 Medina, F. (2008). Catalogue of focal mechanisms of Moroccan earthquakes for the period 1959-2007. ISBN:
309 9954-8347-9-6 [http://www.israbat.ac.ma/wp-content/uploads/2015/03/03-%20Medina%20et%20al.%20\(19-30\).pdf](http://www.israbat.ac.ma/wp-content/uploads/2015/03/03-%20Medina%20et%20al.%20(19-30).pdf)
- 310 Peláez, J.A., M. Chourak, B. A. Tadili, L. Aït Brahim, M. Hamdache, C. López Casado, J. M. Martínez Solares;
311 A Catalog of Main Moroccan Earthquakes from 1045 to 2005. *Seismological Research Letters* 2007;; 78
312 (6): 614–621. doi: <https://doi.org/10.1785/gssrl.78.6.614>
- 313 Simpson, R.W. (1997) Quantifying Anderson's faulting types. *BSSA* 102(B8).
- 314 Townend, J., & Zoback, M. D. (2004). Regional tectonic stress near the San Andreas fault in central and southern
315 California. *Geophysical Research Letters*, 31(15).
- 316 Varryčuk, V. Iterative joint inversion for stress and fault orientations from focal mechanisms. *Geophys. J. Int.*
317 199, 69–77 (2014).
- 318 Walsh, F. R. III, & Zoback, M. D. (2016). Probabilistic assessment of potential fault slip related to injection-
319 induced earthquakes: Application to north-central Oklahoma, USA. *Geology*, 44(12), 991–994.
320 <https://doi.org/10.1130/G38275.1>
- 321 Zoback, M. D. (2010). Reservoir geomechanics. New York: Cambridge University Press.
- 322 Zoback, M.L., First and second-order patterns of stress in the lithosphere: The world stress map project, Jour.
323 *Geophys Res.*, 97, 11,703-11,728, 1992.
- 324
- 325
- 326
- 327
-
- 328

329 **Supporting Information**

330

	Model	Weighting	Friction	N	A ϕ	A ϕ std	SHmax	SHmax std	Mean misfit	Mean dCFS	Oukaimedene misfit	Oukaimedene dCFS	Oukaimedene aux misfit	Oukaimedene aux dCFS	
All mechanisms	0	Inverse distance	0.3–0.9	28	2.16	0.14	177	4	24.6	4.8	5.4	5.8	21.9	27.7	
Exclude Middle Atlas and Eastern High Atlas	1	Inverse distance	0.3–0.9	21	2.07	0.15	2	5	25.5	2.8	1.7	3.6	31.6	21.9	Preferred model
All mechanisms	2	Uniform	0.3–0.9	28	2.11	0.1	162	2	25.6	4.4	9.6	10.8	39.9	26.3	
Exclude Middle Atlas and Eastern High Atlas	3	Uniform	0.3–0.9	21	2.19	0.13	168	4	26.8	3.3	2.4	4.3	24.4	25.6	
Low friction (all mechanisms)	4	Uniform	0.2–0.4	28	2.1	0.12	162	2	25.4	3	9.7	8.4	43.5	12.6	
Low friction (exclude Middle Atlas and Eastern High Atlas)	5	Inverse distance	0.2–0.4	21	1.92	0.17	3	5	23.4	2.2	0.6	4.6	36.5	9.5	
SW planes only (all mechanisms)	6	Uniform	0.3–0.9	28	2.3	0.15	166	2	32.5	17.3	NaN	NaN	27.2	35.1	
SW planes only (exclude Middle Atlas and Eastern High Atlas)	7	Inverse distance	0.3–0.9	21	1.67	0.23	0	3	36.3	15.2	NaN	NaN	23.3	25.6	
SW planes only, low friction (exclude Middle Atlas and Eastern High Atlas)	8	Inverse distance	0.2–0.4	21	1.67	0.24	0	3	36.4	13.2	NaN	NaN	23.7	21.8	
Southern High/Middle Atlas junction, Central and Western High Atlas	9	Inverse distance	0.3–0.9	15	1.85	0.16	2	6	20.3	3.2	8	6.1	36.6	18.9	Too few mechanisms for reliable inversion
Central and Western High Atlas only	10	Inverse distance	0.3–0.9	10	1.75	0.18	5	7	15.6	2.4	11.1	10.3	43.8	16.7	Too few mechanisms for reliable inversion
Western High Atlas only	11	Inverse distance	0.3–0.9	6	1.59	0.24	9	10	7.4	3.5	17.5	9.5	39.6	7.5	Too few mechanisms for reliable inversion

331

332 **Table S1: Summary of alternative models**

333

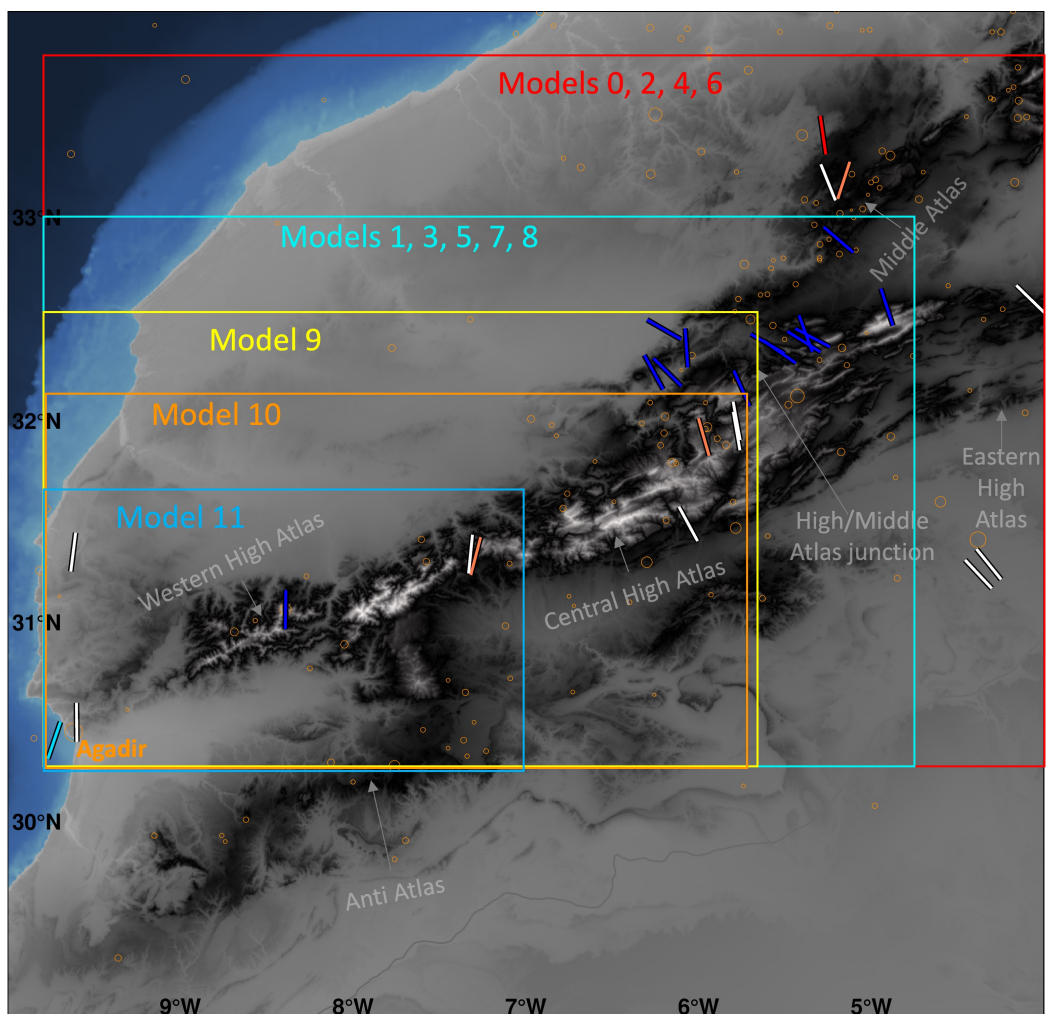
ID	Longitude	Latitude	Depth	Strike, Model 0	Dip, Model 0	Rake, Model 0	Aux Strike, Model 0	Aux Dip, Model 0	Aux Rake, Model 0	Misfit Mech 1, Model 0	dCFS Plane 1, Model 0	Misfit Mech 2, Model 0	dCFS Plane 2, Model 0	Strike, Model 1	Dip, Model 1	Rake, Model 1	Misfit Mech 1, Model 1	dCFS, Model 1
1	-5.97	31.92	10	314.23	63.935	-134.31	200	50	-35	56.2022	2.58496	58.385	2.03365	200	50	-35	50.5522	4.0878
2	-5.75	32.16	11	87.376	28.905	119.03	235	65	75	6.8091	3.04708	43.322	9.97962	87.3756	28.905	119.03	14.7903	2.3641
3	-6.07	32.36	11	114.11	41.41	130.89	245	60	60	5.18833	0.51804	14.057	15.4355	114.107	41.41	130.89	8.42132	0.6155
4	-4.91	32.56	12	225	50	50	97.546	54.068	127.45	15.0249	1.28515	15.893	3.94088	225	50	50	22.3992	0.9
5	-5.78	31.95	12	35.12	80.038	-5.0767	126	85	-170	18.7206	0.30084	43.411	6.51484	35.1196	80.038	-5.0767	13.7767	0.4053
6	-7.29	31.33	16	339.97	69.746	-142.31	235	55	-25	22.4364	4.00881	65.026	6.16172	339.974	69.746	-142.31	26.187	1.0519
7	-7.32	31.34	13	135	90	145	225	55	0	7.24668	3.32386	32.722	1.95398	135	90	145	11.3668	4.6338
8	-5.53	32.34	8.4	35	52	90	215	38	90	37.1972	5.01617	59.7	0.11337	35	52	90	50.1748	4.1086
9	-6.26	32.24	9.1	68.871	30.539	100.26	237	60	84	3.03136	5.29478	45.973	9.74043	68.8712	30.539	100.26	12.7965	3.7293
10	-5.39	32.39	7.6	32	63	90	212	27	90	54.5373	2.38623	64.015	0.63848	32	63	90	65.8298	2.2406
11	-5.38	32.43	5.9	70	25	90	250	65	90	15.0086	7.02912	43.108	23.8485	70	25	90	5.23347	6.2119
12	-5.34	32.41	13.7	28	58	90	208	32	90	49.9457	5.90369	65.639	0.33333	28	58	90	62.9227	4.6643
13	-6.2	32.45	5.2	30	50	90	210	40	90	36.7687	7.42957	62.932	0.23738	30	50	90	50.3065	6.1674
14	-6.18	32.24	5.5	45	50	90	225	40	90	27.966	2.75384	52.389	0.09726	45	50	90	40.322	2.379
15	-5.6	32.38	6.4	30	55	90	210	35	90	44.2433	5.81278	63.501	0.1136	30	55	90	57.4407	4.732
16	-6.06	31.49	33	20.732	76.115	22.699	285	68	165	16.5516	4.98161	21.345	26.9387	20.7319	76.115	22.699	24.0146	4.3327
17	-9.62	31.35	25	322.93	79.169	-169.82	231	80	-11	7.36412	1.09044	20.389	9.54836	322.933	79.169	-169.82	2.77343	1.3693
18	-9.73	30.41	0.2	141.55	67.22	139.25	250	53	29	1.26877	0.41315	27.987	13.4644	141.552	67.22	139.25	3.89291	0.957
19	-5.78	32	23	212	42	16	109.97	79.372	130.88	12.3224	0.19055	1.9433	15.2311	212	42	16	4.52589	0.6468
20	-8.391	31.064	26	121.97	29.358	133.03	255	69	69	5.32089	5.21584	19.815	32.0415	121.967	29.358	133.03	1.70956	3.6102
21	-9.6	30.5	0	44	90	10	314	80	180	5.08449	2.87071	15.486	3.68374	44	90	10	6.53682	0.8038
22	-5.19	32.89	7	190	48	44	67.131	58.92	128.62	21.4968	7.24842	52.119	6.20367	NaN	NaN	NaN	NaN	NaN
23	-5.25	33.17	10	203.5	67.5	11	109.25	79.847	157.12	10.0357	2.02102	24.476	16.0907	NaN	NaN	NaN	NaN	NaN
24	-5.16	33.18	7	334.04	44.125	-158.18	228	75	-48	49.39	3.25653	64.546	6.92859	NaN	NaN	NaN	NaN	NaN
25	-5.28	33.4	12	314.02	47.933	-139.23	194	61	-50	76.4602	2.27383	74.613	5.62258	NaN	NaN	NaN	NaN	NaN
26	-4.32	31.29	5.4	187	69	12	92.644	78.808	158.57	19.9153	12.0207	48.241	26.0603	NaN	NaN	NaN	NaN	NaN
27	-4.38	31.24	8	181	87	18	90.026	72.026	176.85	34.7788	20.3606	72.682	19.5246	NaN	NaN	NaN	NaN	NaN
28	-4.08	32.6	23	182	71	7	89.711	83.383	160.87	36.1615	17.3809	54.449	32.1086	NaN	NaN	NaN	NaN	NaN

334

Table S2: Focal mechanisms

335

336



337

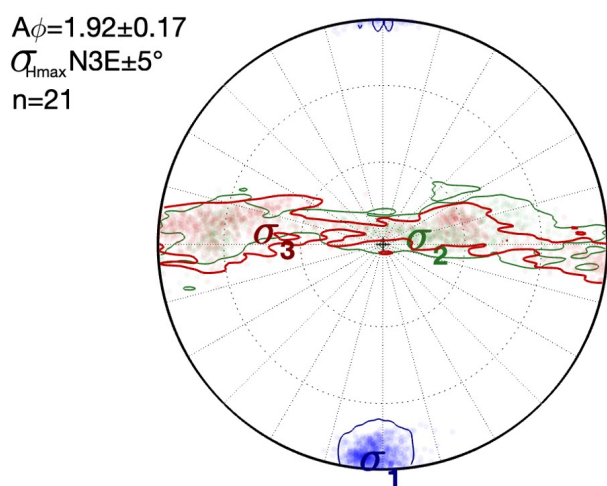
338

339 **Figure S1: Extents of the 11 models examined.** Models 9, 10, and 11 include fewer than 20 focal mechanisms so should
 340 not be considered reliable.

341

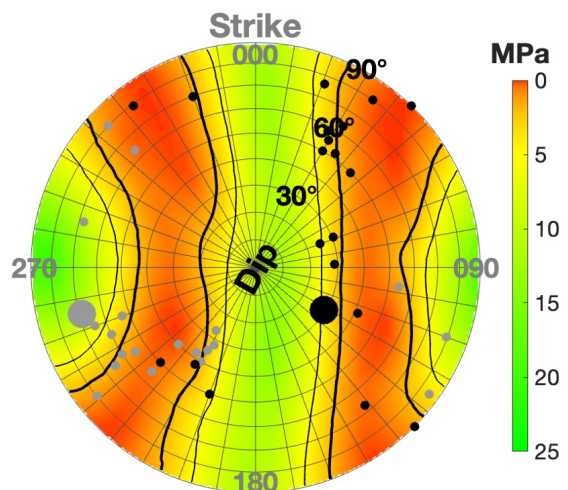
Model 5: Low-friction faults

Stress Inversion Results:
Low friction (0.2–0.4)



342

Fault slip potential:
Low friction (0.2–0.4)



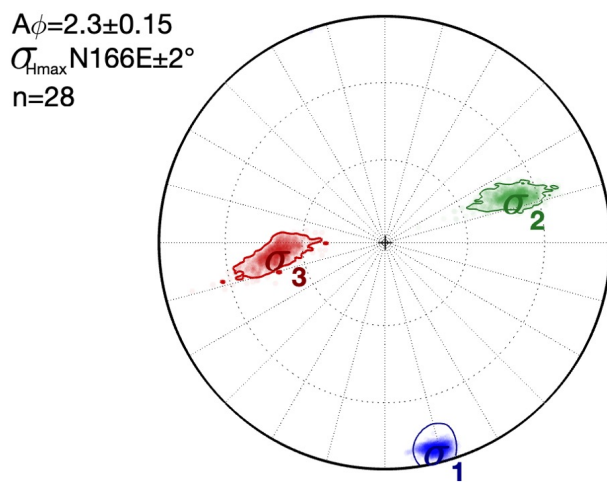
343 **Figure S2: Low-friction faults** Inversion scheme is the same as Model 1 except a random friction 0.2–0.4 is selected for each
 344 of 1001 inversions and FSP models.

345

346

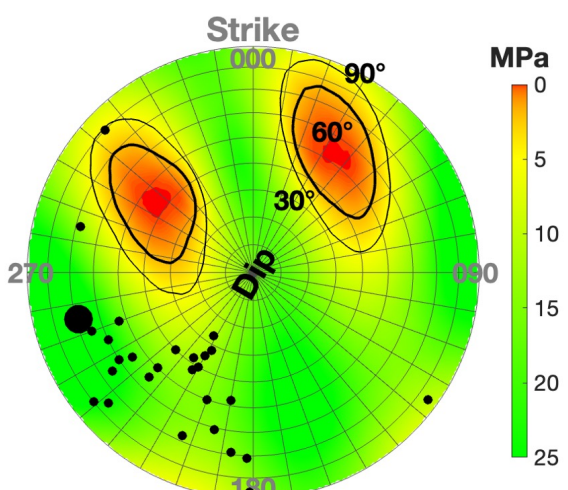
Model 6: SW-striking planes only

Stress inversion results:



347

Fault slip potential:

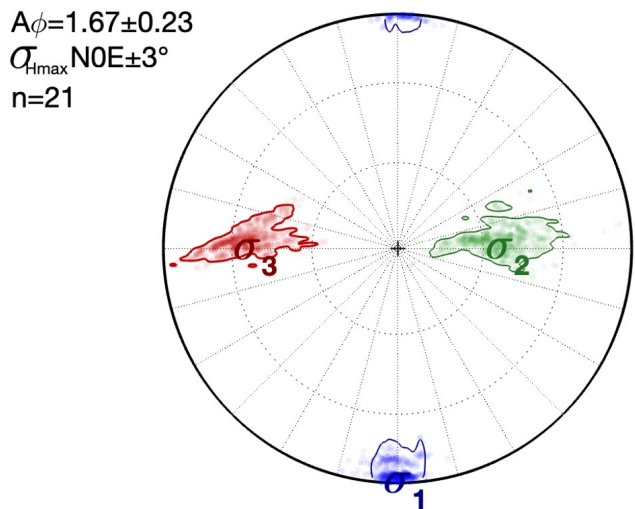


348 **Figure S3: SW-striking focal planes** For each event, the more southwesterly nodal plane is set as the focal plane.

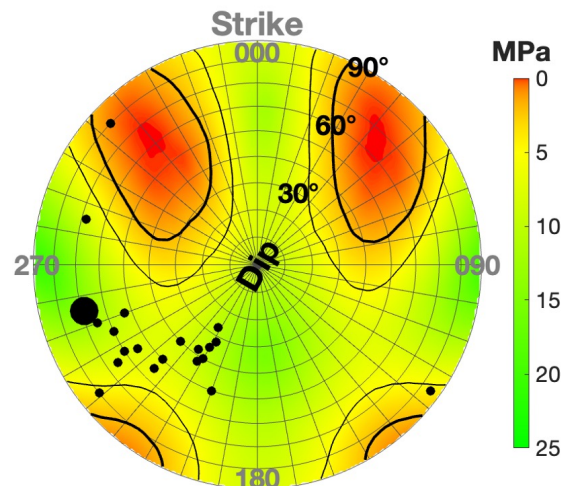
349

Model 8: SW-striking planes only & low friction faults

Stress inversion results:

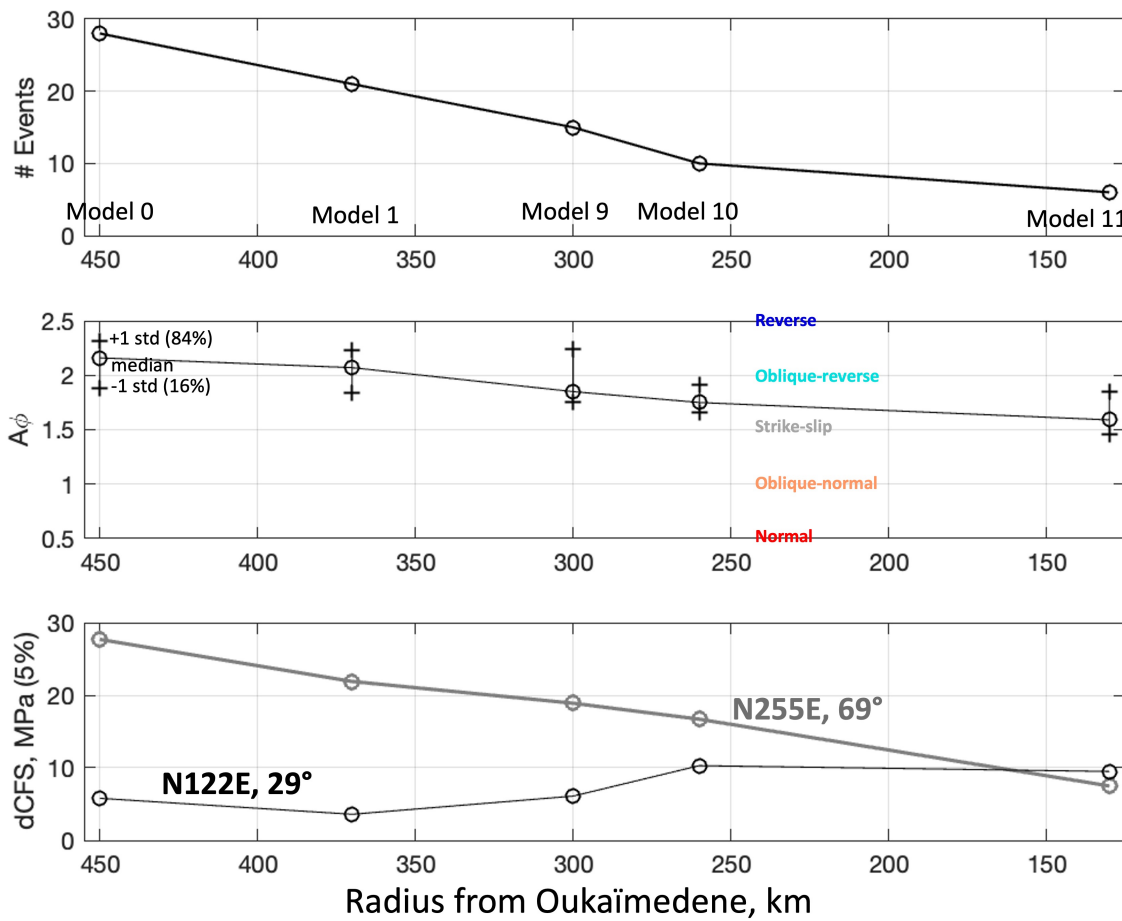


Fault slip potential:



350

351 **Figure S4: SW-striking focal planes with low friction.** For each event, the more southwesterly nodal plane is set as the
352 focal plane. This model also differs from Model 6 (Figure S2) in excluding events from the Middle Atlas and Eastern High
353 Atlas, and in weighting the retained mechanisms by inverse-distance from Oukaïmedene (instead of uniform weights).



354

355 **Figure S6: Inversions with fewer mechanisms.** The area from which focal mechanisms are gathered narrows in on the
 356 Western High Atlas from left to right. (**Top**) The number of focal mechanisms decreases. The associated models are indicated.
 357 (**Middle**) $A\phi$ decreases, suggesting a transition from characteristically reverse-oblique faulting to strike-slip. Circles denote the
 358 median across 1001 inversions; crosses delineate the 16%–84% confidence interval (± 1 standard deviation for normal
 359 distributions). (**Bottom**) The WSW-striking nodal plane becomes progressively better aligned for slip and appears to be as well
 360 oriented as the ESE-striking plane when only the Western High Atlas is considered (Model 11). Models 9, 10, and 11 use too
 361 few focal mechanisms to provide robust results, however.

362

363